Assessment of remotely sensed chlorophyll-*a* concentration in Guanabara Bay, Brazil

Eduardo N. Oliveira
Alexandre M. Fernandes
Milton Kampel
Renato C. Cordeiro
Nilva Brandini
Susana B. Vinzon
Renata M. Grassi
Fernando N. Pinto
Alessandro M. Fillipo
Rodolfo Paranhos

Assessment of remotely sensed chlorophyll-*a* concentration in Guanabara Bay, Brazil

**Eduardo N. Oliveira,[a,]* Alexandre M. Fernandes,[a] Milton Kampel,[b]
Renato C. Cordeiro,[c] Nilva Brandini,[c] Susana B. Vinzon,[d]
Renata M. Grassi,[a] Fernando N. Pinto,[e] Alessandro M. Fillipo,[a] and
Rodolfo Paranhos[e]**

[a]Rio de Janeiro State University, Oceanographic College, Physical Oceanography Department,
Street São Francisco Xavier 524, Rio de Janeiro-RJ, Brazil

[b]National Institute for Space Research, Remote Sensing Division, Avenue dos Astronautas,
1758, São José dos Campos-SP, Brazil

[c]Federal Fluminense University, Institute of Chemistry, Street Outeiro de São João Batista s/n°,
Niterói-RJ, Brazil

[d]Rio de Janeiro Federal University, Program of Ocean Engineering, Technology Center,
Block C—203, Rio de Janeiro-RJ, Brazil

[e]Rio de Janeiro Federal University, Institute of Biology, Avenue Prof. Rodolpho Rocco 211,
Block A, sl. A1-071, Rio de Janeiro-RJ, Brazil

Abstract. The Guanabara Bay (GB) is an estuarine system in the metropolitan region of Rio de Janeiro (Brazil), with a surface area of ~ 346 km^2 threatened by anthropogenic pressure. Remote sensing can provide frequent data for studies and monitoring of water quality parameters, such as chlorophyll-*a* concentration (Chl-*a*). Different combination of Medium Resolution Imaging Spectrometer (MERIS) remote sensing reflectance band ratios were used to estimate Chl-*a*. Standard algorithms such as Ocean Color 3-band, Ocean Color-4 band, fluorescence line height, and maximum chlorophyll index were also tested. The MERIS Chl-*a* estimates were statistically compared with a dataset of *in situ* Chl-*a* (2002 to 2012). Good correlations were obtained with the use of green, red, and near-infrared bands. The best performing algorithm was based on the red (665 nm) and green (560 nm) band ratio, named "RG3" algorithm ($r^2 = 0.71$, chl-*a* $= 62,565 * x^{1.6118}$). The RG3 was applied to a time series of MERIS images (2003- to 2012). The GB has a high temporal and spatial variability of Chl-*a*, with highest values found in the wet season (October to March) and in some of the most internal regions of the estuary. Lowest concentrations are found in the central circulation channel due to the flushing of ocean water masses promoted by pumping tide. © *2016 Society of Photo-Optical Instrumentation Engineers (SPIE)* [DOI: 10.1117/1.JRS.10.026003]

Keywords: chlorophyll-*a* concentration; optical properties; ocean color empirical algorithm; Medium Resolution Imaging Spectrometer; Guanabara Bay.

1 Introduction

According to the classification introduced by Ref. 1, the overall ocean waters are partitioned in case-1 and case-2 waters. Case-1 waters are those in which the ocean color depends mainly on phytoplankton biomass and can be described in terms of the chlorophyll-*a* concentrations (Chl-*a*). In this case, algorithms that make use of the bands centered in the blue–green region of the electromagnetic spectrum have been successfully applied to estimate.[2] However, these algorithms are not suitable for case-2 waters,[3,4] usually found in coastal regions, where other optically active constituents, such as colored dissolved organic matter (CDOM), inorganic particles and detritus, do not necessarily covary with Chl-*a*. Consequently, the estimation of

Chl-*a* as an index of phytoplankton biomass in optically complexity waters (case-2) is not a trivial task.[5] Among the biggest challenges are the lack of appropriate models of atmospheric correction to derive precisely the remote sensing reflectance (R_{rs}) and the absence of robust bio-optical inversion methods to differentiate Chl-*a* from other optically active constituents.[5] A variety of atmospheric correction models[5,6–12] and bio-optical inversion methods[5,13–15] have been proposed and evaluated in the scientific literature. To overcome the difficulties in estimating Chl-*a* in case-2 waters, new approaches have been adopted[16–20] using spectral bands centered in the red and infrared region of the electromagnetic spectrum. A comprehensive review of different types of algorithms, their applications, and their limitations for monitoring algae blooms is discussed in Ref. 21.

The Guanabara Bay (GB) is an estuarine system located in the metropolitan region of the state of Rio de Janeiro, Brazil (Fig. 1), with a surface area of 346 km^2, average depth of ~7 m, river inflow of ~100 m^3 s^{-1} and semidiurnal tide with mean amplitude of ~0.8 m that associated with the local currents promotes about 50% water renewal in ~11 days.[22] Tidal currents at the bay entrance range from 80 to 150 cm s^{-1}.[23] The bay receives liquid and solid contributions of industries, including two oil refineries, oil terminals, two commercial ports, and many shipyards, among other economic activities. GB is under the regime of a humid tropical climate and presents a spatial gradient of eutrophication from the mouth to the bay head.[24–26] Due to the large amount of organic matter and debris and its highly eutrophic character, the transparency of GB waters is extremely low, especially in innermost regions, with average "Secchi" depth values ≤1 m.

On account of the large spatial and temporal variability caused by local circulation pattern and the inputs from 27 sub-basins of the GB watershed, a large number of sampling points are required for an adequate monitoring of the water quality. Alternatively, a remote sensing approach can provide low-cost synoptic analyses with high temporal resolution. Of particular interest are the radiometric data collected by ocean color sensors, such as Moderate Resolution Imaging Spectroradiometer (2002 to current) and Medium Resolution Imaging Spectrometer (MERIS, 2002 to 2012), both with temporal resolution of 1 to 2 days and global coverage. Recent scientific publications have demonstrated the possibility of monitoring water quality in coastal areas and estuarine systems using these sensors.[4,17–19,27–32]

Previous studies using satellite data for assessing the water-quality parameters in GB have used LANDSAT thematic mapper (TM) and enhanced thematic mapper (ETM+) sensors.[33,34] TM and ETM+ data were shown to be adequate to analyze Secchi depth, total suspended solids, and turbidity, but no correlation was found with Chl-*a* concentrations and sensor bands in the GB.[33] The TM and ETM+ limitations are due to the relatively low signal-to-noise ratio[35] as well as to the limited number of spectral bands in the visible region, where water-quality spectral signatures are observed.
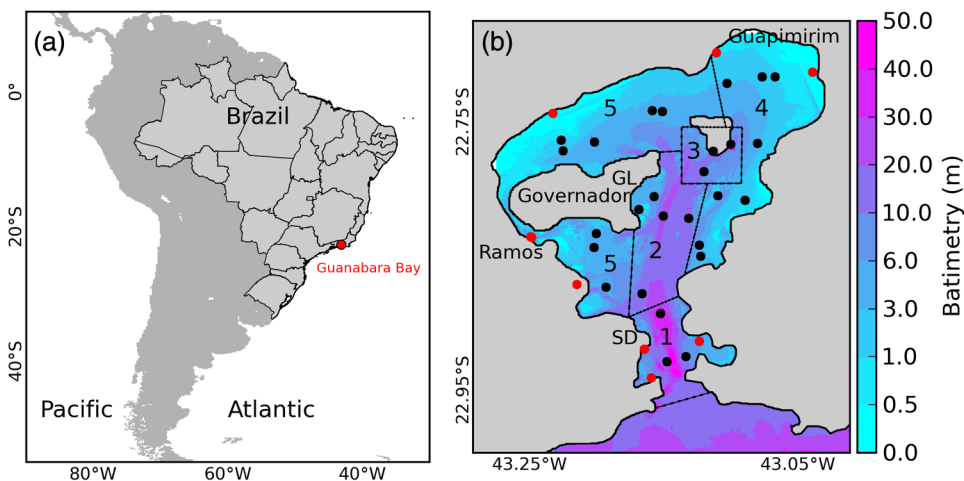

Fig. 1 (a) South America, Brazil, Guanabara Bay; (b) general view of Guanabara Bay and the sampling stations (black and red dots). The red circles in (b) show the sample points located at the marginal regions. SD and GL are meteorological stations at Santos Dumont and Galeão airports, respectively.

The present study aims to develop an empirical algorithm to identify the spatial/temporal distribution of Chl-*a* concentration patterns in the GB. To do so, a time series of *in situ* Chl-*a* is compared against MERIS-derived estimates using different band-ratio algorithms. In order to facilitate the interpretation of the results, GB was divided into five sectors: S1, S2, S3, S4, and S5 (Fig. 1). S1 and S2 sectors enclosed the tidal channel, where the highest intrusion of ocean waters occurs. S3 sector encloses some islands with shallower depths in comparison with sectors S1 and S2 and less influenced by tidal currents. Currents are weaker on S4 sector, but it is under a more substantial river inflow influence on its northeast (more preserved) and east (more impacted by human activities) portions. S5 sector also has a significant contribution of river inputs in its northwestern portion, and tidal current values are comparable to S4. S5 sector receives the most drastic contribution of municipal and industrial outfalls and is the most impacted by anthropogenic activities.[26]

2 Available Data and Analysis Procedures

2.1 *In Situ Chlorophyll-a Concentration*

A dataset with 570 measurements of Chl-*a*, collected between October 2002 to January 2012, was provided by the Laboratory of Hydrobiology, Rio de Janeiro Federal University.[36] Surface water samples (depth < 1 m) were collected at 35 sampling sites distributed in different sectors of GB (Fig. 1).

Approximately one sample per month was collected for each sector. The samples were filtered using cellulose membrane filters (Millipore HAWP 0.45 μm) immediately after collection, and the filters were stored in liquid nitrogen. The Chl-*a* was determined after extraction in 90% acetone over a period of 18 h at 4°C. Both measures (scanning spectrophotometer Perkin-Elmer Lambda 25) and calculations were based on procedures and equations described by Ref. 37. The spectrophotometer was calibrated with pure Chl-*a* (Sigma ® C-6144) and the detection limit estimated at 0.02 mg m^{-3}.[38]

2.2 *Photosynthetically Available Radiation and Precipitation Rate*

Monthly rainfall data collected at two meteorological stations (22°48′S to 43°15′ W and 22°54′ S to 43°09′ W, Fig. 1) was made available by the Institute of Air Control of the "Santos Dumont and Galeão" airports. Precipitation data in the GB watershed area were derived from the Tropical Rainfall Measuring Mission (TRMM 3B43 product). Both PAR and TRMM precipitation data were downloaded from Giovanni/NASA[39] with spatial resolution of 0.25×0.25 deg.

2.3 *Medium Resolution Imaging Spectrometer Image Processing*

Atmospherically corrected MERIS full-resolution Level 2 images were provided by the CoastColour Project Group,[40] with a spatial resolution of 300 m, from January 2003 to April 2012. The atmospheric correction scheme is supported by a neural network, named Case 2 Regional Processor (C2R), applicable to a wide range of water types, from clear to extremely turbid water.[41,42] The BEAM software[43] and the Python programming language[44] were used for the manipulation of MERIS images as well as for the extraction of the remote sensing reflectance (R_{rs}). Three criteria guided the extraction of R_{rs}: (1) time lag of up to ± 4 h between the satellite overpass and *in situ* Chl-*a* measurement; (2) a window of 3×3 pixels centered at the sampling points for R_{rs} median value; and (3) after discarding the pixels associated with several quality control flags such as cloud cover, sun glint, pixels adjacent to land or clouds and so on, the MERIS data were only validated when the number of valid pixels in the 3×3 window was ≥ 4.

3 Algorithm Development

Various combinations of MERIS band ratios were initially selected from the literature and correlated with *in situ* Chl-*a* for obtaining the regression curves and deriving empirical algorithms, as described below.

3.1 Ocean Color 3-Bands e-Ocean Color 4-Bands

The Ocean Color 3-band (OC3) and Ocean Color-4 band (OC4) algorithms[2] make use of the blue and green bands to estimate the global Chl-*a*. Due to the significant contribution of CDOM and nonalgal particles in the spectral region of the blue, the algorithms tend to overestimate Chl-*a* in Case-2 waters. To check the correlation between the OC3 and OC4 algorithms with *in situ* Chl-*a*, the following relationships were used:

$$OC3 = \frac{\max[R_{rs}(442), R_{rs}(489)]}{R_{rs}(559)}, \tag{1}$$

$$OC4 = \frac{\max[R_{rs}(442), R_{rs}(489), R_{rs}(509)]}{R_{rs}(559)}, \tag{2}$$

where R_{rs} = remote sensing reflectance and max means the maximum ration of the spectral bands.

3.2 Fluorescence Line Height and Maximum Chlorophyll Index

Suitable for biomass estimates in waters with moderately high Chl-*a* (> 0.5 mg m^{-3}), the fluorescence line height (FLH)[45,46] makes use of the chlorophyll fluorescence peak centered at 680 nm, based on an interpolated line between 665 and 708 nm:

$$FLH = R_{rs2} - \left[R_{rs1} + \left(\frac{R_{rs3}}{-} \atop R_{rs1} \right) * \frac{(\lambda_2 - \lambda_1)}{(\lambda_3 - \lambda_1)} \right], \tag{3}$$

where R_{rs} = remote sensing reflectance, $\lambda_1 = 665$ nm, $\lambda_2 = 680$ nm, $\lambda_3 = 708$ nm.

When the Chl-*a* increases significantly, part of the fluorescence signal at 680 nm is impacted by the magnification of the chlorophyll absorption band in 670 nm. In this case, the reflectance spectrum has a maximum peak at 700 nm and minimum at 665 and 680 nm. The maximum chlorophyll index (MCI)[46,47] makes use of these features and it is recommended for high Chl-*a*, >30 mg m^{-3}:

$$MCI = R_{rs2} - \left[R_{rs1} + (R_{rs3} - R_{rs1}) * \frac{(\lambda_2 - \lambda_1)}{(\lambda_3 - \lambda_1)} \right], \tag{4}$$

where R_{rs} = remote sensing reflectance, $\lambda_1 = 680$ nm, $\lambda_2 = 708$ nm, $\lambda_3 = 753$ nm.

3.3 Near-Infrared-Red Model

The near-infrared (Nr) model takes into account the relationship established between R_{rs} and the optical properties of water:

$$R_{rs} \propto \frac{f}{Q} * \left[\frac{b_b}{(a + b_b)} \right], \tag{5}$$

where a and b_b are the absorption and backscattering coefficients, respectively, and f/Q ratio describes the dependence of R_{rs} relative to the water column emergent light field.[48] Using strategically placed spectral bands, the model seeks to minimize the contributions of different constituents (other than Chl-*a*) to the absorption and also minimize the backscattering of suspended particulate matter, maximizing the model sensitivity to variations of Chl-*a*. The Nr model is used for assessing Chl-*a* in turbid productive waters with Chl-*a* ≥ 5 mg m^{-3}.[16,49] Further details of the relationships established in the Nr model are discussed in the scientific literature.[49–52]

Four variations of the Nr model were implemented in this work using MERIS spectral bands:[16,18,49,50]

$$\text{Nr1} = \frac{R_{\text{rs}}(708)}{R_{\text{rs}}(665)}, \tag{6}$$

$$\text{Nr2} = \left[\frac{1}{R_{\text{rs}}(665)} - \frac{1}{R_{\text{rs}}(708)}\right] * R_{\text{rs}}(753), \tag{7}$$

$$\text{Nr3} = \left[\frac{1}{R_{\text{rs}}(665)} - \frac{1}{R_{\text{rs}}(680)}\right] * R_{\text{rs}}(708), \tag{8}$$

$$\text{Nr4} = \frac{[R_{\text{rs}}(665)^{-1} - R_{\text{rs}}(680)^{-1}]}{[R_{\text{rs}}(708)^{-1} - R_{\text{rs}}(680)^{-1}]}, \tag{9}$$

where R_{rs} = remote sensing reflectance.

3.4 Red–Green Model

Red–green (RG) model makes use of red and green bands to derive Chl-*a*.[17,19,53–55] Four variants of RG model were tested in the present work, considering the inclusion of the 708-nm band in one of those in Eq. (10):

$$\text{RG1} = \frac{\max[R_{\text{rs}}(680), R_{\text{rs}}(708)]}{R_{\text{rs}}(560)}, \tag{10}$$

$$\text{RG2} = \frac{R_{\text{rs}}(665)}{\max[R_{\text{rs}}(560), R_{\text{rs}}(620)]}, \tag{11}$$

$$\text{RG3} = \frac{R_{\text{rs}}(665)}{R_{\text{rs}}(560)}, \tag{12}$$

$$\text{RG4} = \frac{[R_{\text{rs}}(665) + R_{\text{rs}}(680)]}{[R_{\text{rs}}(560) + R_{\text{rs}}(620)]}, \tag{13}$$

where R_{rs} refers to remote sensing reflectance.

4 Statistical Analysis

Statistical comparisons between *in situ* measured Chl-*a* and estimated Chl-*a* from MERIS images were based on the following error parameters: Spearman's correlation coefficient (R^2), root mean square error (RMSE) and mean relative error (MRE):

$$\text{RMSE} = \sqrt{\frac{1}{n}\sum(\text{Chl-}a_{\text{estimated}} - \text{Chl-}a_{in\,situ})^2}, \tag{14}$$

$$\text{MRE}(\%) = \frac{\text{Chl-}a_{\text{estimated}} - \text{Chl-}a_{in\,situ}}{\text{Chl-}a_{in\,situ}} * \frac{100}{n}, \tag{15}$$

where n is the total number of observations.

5 Results and Discussion

5.1 *In Situ Chlorophyll-a*

For a total of $n = 570$ measurements of Chl-*a*, the concentrations mean, standard deviation, median, minimum and maximum values were 65.1, 101.8, 34.9, 1.0, 974.0 mg m^{-3}, respectively, while the corresponding seasonal totals were 80.5, 129.3, 38.8, 1.0, 974.0 mg m^{-3} ($n = 258$) for the wet season (October to March), and 52.4, 69.0, 30.6, 1.4, 736.4 mg m^{-3} ($n = 312$) for the dry season (Table 1). Mean Chl-*a* and "Secchi" depths in GB show seasonality in the different sectors (Fig. 1). The wet season is characterized by higher Chl-*a* values (lower Secchi depths) and the dry season by lower Chl-*a* values (higher Secchi depths) (Table 1). The only exception was found in S4 sector, which has slightly higher mean Chl-*a* in the dry season (71.4 mg m^{-3}) compared to the wet season (66.1 mg m^{-3}). The same result is observed when one considers the median values of Chl-*a* (Table 1). Chl-*a* standard deviation (Std) is higher in the wet season (Table 1) as well as the coefficient of variation (CV = Std/mean). On the wet season, the CV for sectors S1, S2, S3, S4, and S5 was 114%, 71%, 136%, 182%, and 125%, respectively. In the dry season, CV corresponded to 97%, 78%, 77%, 98%, 110%, indicating high variability of the data, mainly in the wet season. In general, highest Chl-*a* values are observed in summer and tidal outflow conditions and lower values during winter conditions and tidal inflow.[22,24,25]

Eight Chl-*a* extreme values ($n_e = 8$, >500 mg m^{-3}) were identified in sectors S3, S4, and S5 ($n_e = 1, 1,$ and 6, respectively). Seven of them were identified in the wet season. The wet season has intense insolation, higher nutrient input from river discharge (not available) and stronger temperature/salinity gradients due to increased stratification of the water column,[24] conditions that are favorable for blooming.[56] Four out of eight extreme values were measured along the western circulation channel located between Governador Island and Ramos beach (Fig. 1),

Table 1 *In situ* Chl-*a* mean values and *Secchi* depths at different sectors of Guanabara Bay from 2002 to 2012 (see Fig. 1 for sectors).

Sector	No. of obs.	Chlorophyll (mg m^{-3})					Secchi depth (m)				
		Mean	Median	Std	Min	Max	Mean	Median	Std	Min	Max
Wet season (January, February, March, October, November, December)											
S1	62	29.1	21.6	33.3	1.0	188.1	1.9	1.9	1.0	0.5	5.0
S2	39	40.9	29.7	29.2	3.4	140.1	1.3	1.5	0.4	0.5	2.5
S3	28	86.4	50.8	118.3	6.8	559.9	0.9	1.0	0.5	0.5	3.0
S4	44	66.1	46.0	120.4	14.1	829.1	0.7	0.7	0.2	0.1	1.5
S5	85	141.6	87.4	177.9	1.4	974.0	0.6	0.5	0.3	0.2	1.5
	258	80.5	38.8	129.3	1.0	974.0	1.1	1.0	0.8	0.1	5.0
Dry season (April, May, June, July, August, September)											
S1	76	14.8	10.3	14.4	1.4	57.0	3.0	3.0	1.2	0.8	7.5
S2	49	32.7	26.2	25.8	2.6	96.0	2.0	1.5	1.2	0.6	7.0
S3	37	39.2	31.3	30.3	6.0	142.8	1.2	1.0	0.6	0.5	3.0
S4	50	71.4	50.7	70.5	11.1	371.0	0.9	1.0	0.3	0.3	2.0
S5	100	86.1	63.4	95.2	1.7	736.4	0.7	0.7	0.5	0.1	3.9
	312	52.4	30.6	69.0	1.4	736.4	1.6	1.0	1.2	0.1	7.5
Global	570	65.1	34.9	101.8	1.0	974.0	1.3	1.0	1.1	0.1	7.5

one of the most impacted marginal regions in the GB.[25] The 300-m spatial resolution of the MERIS sensor is not apropriated to study this small channel. The lack of information about the spatial extent of these extreme concentrations (both vertically and horizontally) restricts a more detailed analysis about the impact on primary productivity. It should be noted that at the time of water sampling, the station location can be moved in the presence of local spots of intense bloom. The distribution pattern of these blooms is a problem for remote sensing, as the phytoplankton concentrations can vary by more than 1 order of magnitude within the instantaneous field of view (IFOV) of the orbital sensor. Global mean Chl-*a* of 65.1 mg m^{-3} (Table 1) reduces to a value of 55.7 mg m^{-3} when removing the extreme values, considered here as outliers.

5.2 Total Suspended Matter and Particulate Organic Matter

To support the analysis, previous studies about total suspended matter (TSM) were assessed from the scientific literature.[26,33,57,58] The average TSM concentrations found within GB region were relatively low, usually <50 g m^{-3} with higher concentrations in the inner portion and during wet season. This pattern highlights the role of primary productivity and dissolved organic matter in the degree of turbidity in the bay, which presents an overall Secchi depth of ~1.0 m in average (Table 1). Particulate organic matter (POM) is predominantly composed of organic matter of indigenous origin and the contribution of land-based sources for POM is more relevant in the wet season.[58]

5.3 Reflectance Spectrum

A total of 162 match-ups were extracted from 26 MERIS images. The R_{rs} spectra varied significantly in the visible and NIR regions (Fig. 2). In general, there is an increasing exponential curve from 412 to 560 nm, and high peaks in R_{rs} at 708 nm, typical of waters with high Chl-*a*.[51,59] The lack of *in situ* radiometric data and concomitant information about the concentrations of other optically active constituents (TSM, POM, and CDOM) precludes a more detailed assessment of the contribution of these constituents to the R_{rs} spectrum.
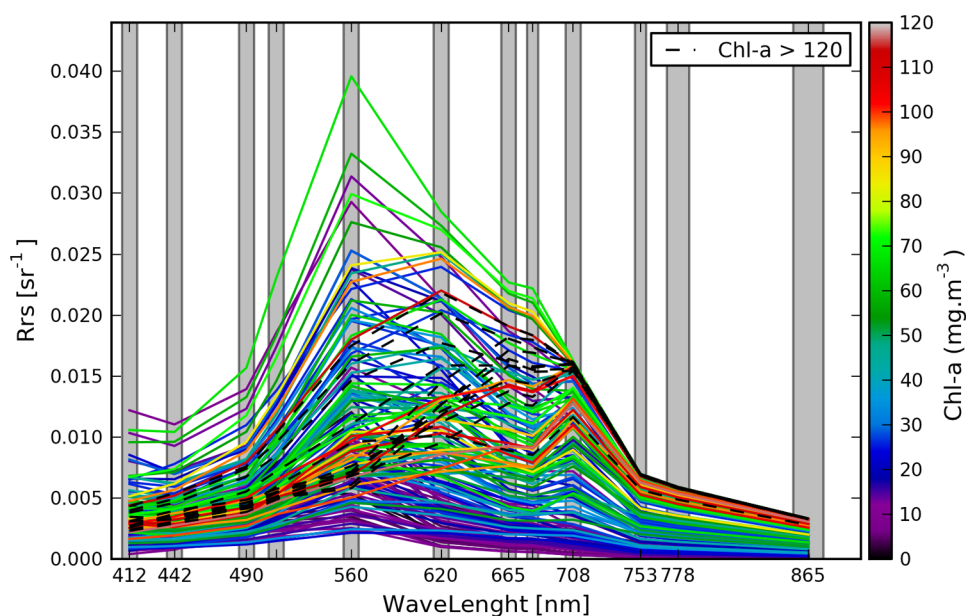

Fig. 2 Remote sensing reflectance derived from MERIS full-resolution images concomitant with *in situ* Chl-*a* concentrations (match-up: *n* = 162, derived from 26 MERIS images). The gray bars delimit the spectral bands of MERIS sensor.

5.4 Ocean Color-3 Band, Ocean Color-4 Band, Fluorescence Line Height and Maximum Chlorophyll Index Chlorophyll-a Algorithms

The scattering of points in Fig. 3(a) highlights the lack of correlation between Chl-a and OC3 [Eq. (1)] and Chl-a and OC4 [Eq. (2)]. The dissolved organic matter in the GB has impact in the shorter wavelengths and restricts the use of algorithms that use the blue/green ratio. The algorithm MCI [Eq. (3)] shows an improved performance, $R^2 = 0.55$, when compared to FLH [Eq. (4)], $R^2 = 0.21$ but still with a large dispersion of points [Fig. 3(b)].

5.5 Near-Infrared and Red–Green Chlorophyll-a Algorithms

Figure 4 shows the relations between *in situ* Chl-a and the index determined by the Nr algorithms [Eqs. (6) and (7)] and RG algorithms [Eqs. (10) to (13)]. The wet season had a lower number of match-ups, 46, whereas the dry season had 116. The results derived from Eqs. (8) and (9) are not shown due to the poor correlation observed among Chl-a, Nr3, and Nr4 ($R^2 = 0.01$ and 0.13, respectively). The algorithms that used only the red and infrared bands [Nr1 and Nr2, $R^2 = 0.46$ and 0.44, Figs. 4(a) and 4(b), respectively] did not show satisfactory performance. Though, in others regions, the Nr model has been successfully used for case 2 waters with high Chl-a.[16,18,19,51,60] Previous works already discussed about the difficulties of C2R atmospheric correction algorithm to estimate the reflectance peak at 708-nm MERIS band with increasing Chl-a.[60,61] It is interesting to observe that the algorithms, which make use of one or two infrared bands, FLH, MCI, Nr1, Nr2, Nr3, Nr4 [Eqs. (3), (4), and (6)–(9), respectively], did not have a good performance, except the RG1 [Eq. (10)] that has the green and red band too. Atmospheric correction is yet a challenge and one of the most limiting factors for an accurate observation of water constituents from satellite remote sensing data, particularly in water masses dominated by significant concentrations of phytoplankton and CDOM.[62,63]

However, phytoplankton absorption influences the radiation that leaves the water in a nonlinear way.[64,65] The absorption of light by phytoplankton causes the phenomenon of light emission (fluorescence), and the fluorescence maximum peak correlates positively with Chl-a. For Chl-$a < 10$ mg m^{-3}, the fluorescence peak is located at ~685 nm, but shifts to longer wavelengths with increasing concentration (red shift), reaching 715 nm when Chl-$a \geq 100$ mg m^{-3}.[54] Several factors can difficult the interpretation and quantification of fluorescence signal as a function of Chl-a: (i) the fluorescence signal may saturate at high Chl-a; (ii) the physiological state of the phytoplankton cells; (iii) the photo inhibition of phytoplankton due to intense solar radiation; (iv) the presence of photoprotective pigments, which may increase the absorption of light in the spectral region of blue–green, with no corresponding increase in fluorescence signal; (v) the package effect that makes larger phytoplankton cells has lower absorption per unit mass of Chl-a than smaller cells; or (vi) indirect effects caused by
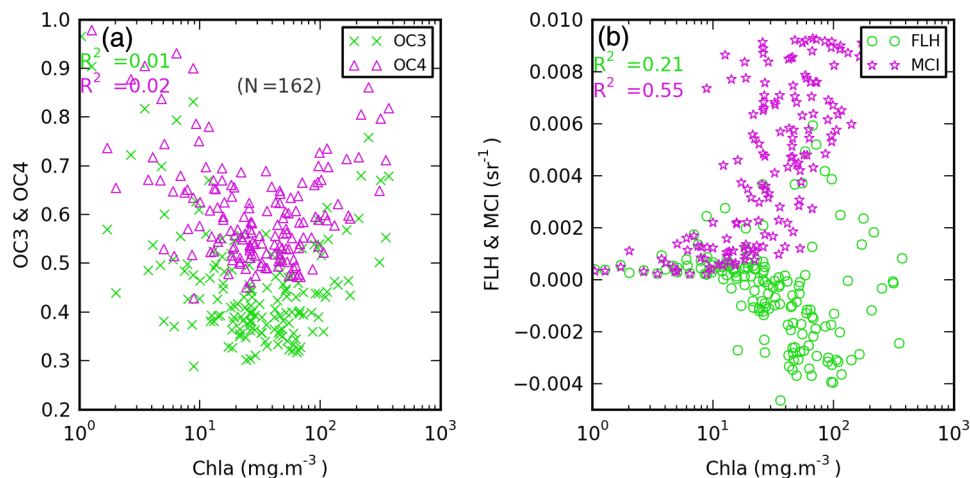

Fig. 3 *In situ* Chl-a (mg m^{-3}) versus (a) OC3 and OC4 algorithms; (b) FLH and MCI algorithms.
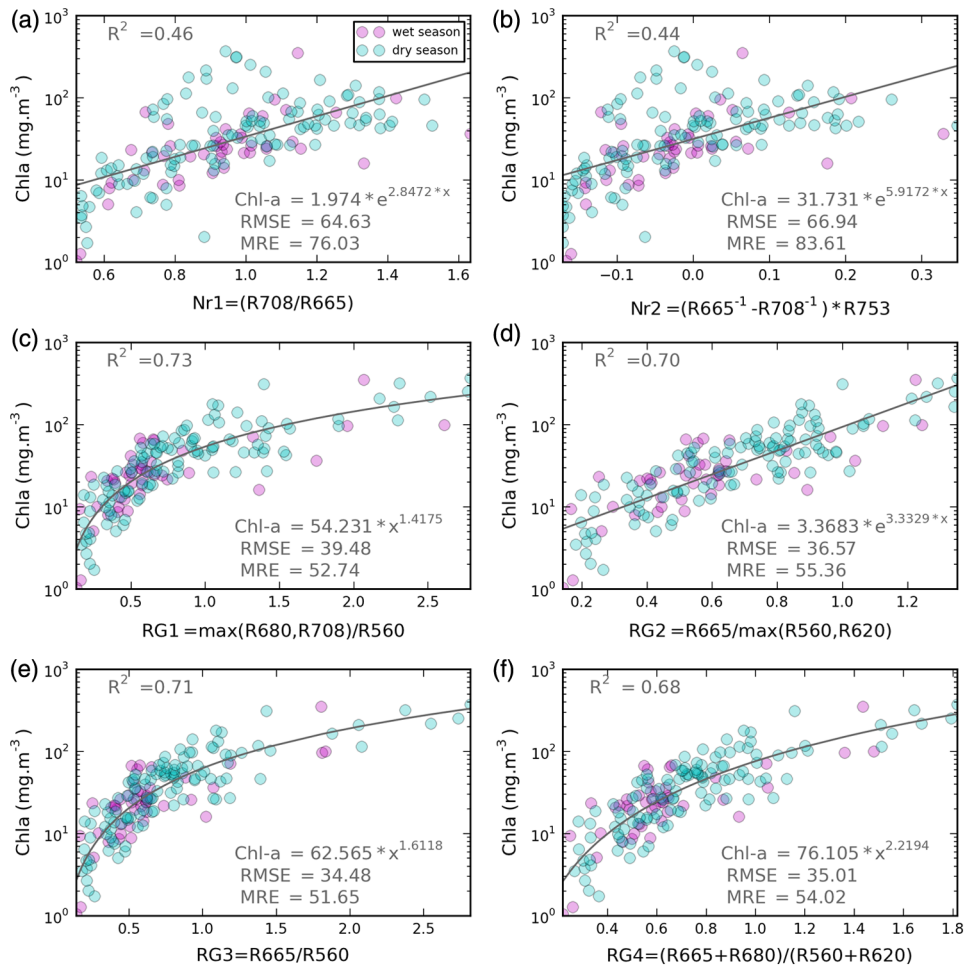
Fig. 4 *In situ* Chl-*a* (mg m^{-3}) versus algorithms (a) Nr1; (b) Nr2; (c) RG1; (d) RG2; (e) RG3; (f) e RG4, according to Eqs. (6), (7), (10)–(13), respectively. Number of match-ups = 162 (from 26 MERIS full-resolution images), 46 for wet and 116 for dry season.

CDOM absorption, which can reduce the availability of light absorbed by the phytoplankton in the spectral region of blue–green, impacting the fluorescence signal per unit of Chl-*a*.[54,64–66]

Due to the package effect and phytoplankton pigment composition, the values of Chl-*a* specific absorption coefficient of phytoplankton (a_{ph}^*, absorption coefficient of phytoplankton per unit of Chl-*a* concentration) in all parts of the spectrum as well as the variability of a_{ph}^* decreases with increasing Chl-*a*.[66] The variability of a_{ph}^* depends on the physiological and ecological dynamics of the phytoplankton community and can be a source of uncertainty in models for the remote estimation of Chl-*a*.[51] Gilerson et al.[67] simulated around 2000 reflectance spectra for a wide range of typical conditions for inland and coastal waters and found that the variability of a_{ph}^* is the major factor that affect the performance of the Nr model. The driving phytoplankton assemblages of GB are typical for eutrophic to hypertrophic systems, largely dominated by blooms and also red tide forming nanoplankton, filamentous cyanobacteria and microplankters.[57,68] Thus, in order to check the Nr model performance, studies for the variability of phytoplankton absorption properties need to be carried out for this study area.

The algorithms based on RG model showed better results [Figs. 4(c)–4(f)]: RG1 ($R^2 = 0.73$), RG2 ($R^2 = 0.70$), RG3 ($R^2 = 0.71$), and RG4 ($R^2 = 0.68$). First, due to the good performance of C2R atmospheric correction to derive the R_{rs} in the region of blue and green[60] and second, because of the red/green band ratio and its tolerance to atmospheric correction errors.[17] Some factors can produce inconsistencies in the calibration process of bio-optical algorithms, such as: (i) changes in Chl-*a* due to time lag between *in situ* Chl-*a* and the satellite overpasses, (ii) high spatial variability of the Chl-*a*, making the *in-situ* sampling not representative of the area covered

by the orbital sensor IFOV, or (iii) problems with atmospheric correction. In any case, such inconsistencies are difficult or even impossible to be identified without the support of *in-situ* data or real-time knowledge of field conditions.

Recent work developed in estuarine regions with characteristics similar to GB (optical properties modulated mainly by phytoplankton and CDOM) made use of green and red bands to quantify the Chl-a. Le et al.[17] and Tzortziou et al.[69] showed that there is strong correlation between Chl-a and red/green ratio on Chesapeake Bay and Tampa Bay, respectively. The question is how the optical properties of water (R_{rs}, absorption and scattering coefficients) are controlled by the optical constituents (Chl-a, CDOM, and inorganic particles). In both cases, Chesapeake Bay and Tampa Bay, the total absorption in the spectral region of green and red bands shows strong correlation with Chl-a. On the other hand, in case-2 waters where absorption is dominated by the inorganic particles, as in the Gironde estuary[70] and Yangtze estuary,[71] algorithms making use of the red/green ratio cannot provide satisfactory results.

In the GB, the high loads of dissolved organic matter and particulate organic matter, composed predominantly by organic matter from autochthonou source,[58] in association with high Chl-a, characterize an environment where the application of red/green algorithms is promising. Nevertheless, the presence of dissolved organic matter can be an issue. According to Ref. 72, CDOM absorption at 700 nm is no longer negligible when $a_{CDOM}(400\ nm) > 2\ m^{-1}$. The lack of *in-situ* data of other optically active constituents and other optical properties of the aquatic environment restricts the design of an anticipated scope (dominant constituents, concentration range, covariances, adequacy of the atmospheric correction algorithm) that could support the elaboration and implementation of a bio-optical algorithm in the GB.

Due to the improved statistical performance, the algorithm chosen to estimate the Chl-a using MERIS images was the RG3 [Eq. (12), Fig. 4(e)] ($R^2 = 0.71$, RMSE = 34.48; MRE = 51.65%):

$$Chl\text{-}a = 62.565 * x^{1.6118}, \tag{16}$$

where $x = R_{rs}(665)/R_{rs}(560)$. The algorithm RG1 [Eq. (10) and Fig. 4(c)] had a better correlation, $R^2(0.73)$ but with higher RMSE and MRE values (39.48% and 52.74%) and higher scattering with high Chl-a [Fig. 4(c)].

The RG3 algorithm was adjusted for a better fitting with the GB *in situ* Chl-a data ($1 \leq Chl\text{-}a \leq 500\ mg\ m^{-3}$) and MERIS data. Table 2 shows the mean values and other Chl-a statistc parameters of the dataset used to fit the RG3 algorithm. As can be seen in Fig. 4(e), the algorithm detection limit was ~3 mg m^{-3}.

5.6 *In Situ Chl-a and Satellite-Derived Chlorophyll-a Time-Series*

The algorithm RG3 [Eq. (16)] was applied to the MERIS set of images from January 2003 to April 2012. Time series of monthly average Chl-a concentrations, derived from samples collected *in situ*, and estimated from MERIS image (Chl-a MERIS) were obtained. A mask of 3 pixels was applied over the MERIS images in order to account for the shallow bottom. This masked pixels were excluded from the data comparison or other analyses. Disregarding the sample points located in the masked areas (red circles, Fig. 1) and the sample points with extreme concentrations (Chl-a > 500 mg m^{-3}, see Sec. 5.1), the global average *in-situ* Chl-a (both dry and wet seasons) changed from 21.2, 36.3, 59.5, 68.9, 111.6 mg m^{-3} to

Table 2 *In situ* Chl-a mean values used to fit the RG3 algorithm (match-up with MERIS image).

Season	No. of obs.	Chlorophyll (mg m^{-3})				
		Mean	Median	Std	Min	Max
Wet	46	36.3	24.0	52.6	1.0	351.5
Dry	116	57.0	42.1	65.7	1.7	317.0

Table 3 Global *in situ* Chl-*a* mean values (both dry and wet seasons) for each sectors (Fig. 1).

Sectors	Chlorophyll (mg m^{-3})	Chlorophyll (mg m^{-3})[a]
S1	21.2	22.1
S2	36.3	36.3
S3	59.5	47.0
S4	68.9	54.3
S5	111.6	72.1

[a]Disregarding the sample points located in the masked areas (red circles, Fig. 1) and the sample points with extreme concentrations (Chl-*a* > 500 mg m^{-3}, see Sec. 5.1).

22.1, 36.3, 47.0, 54.3, 72.1 mg m^{-3} (sectors S1, S2, S3, S4, and S5, respectively, Fig. 1), as can be seen in Table 3.

In the GB (mean depth ~7.0 m), the bottom reflectance is avoided due to the low Secchi depth (global mean Secchi depth 1.3 m, Table 1). Particulary, the mean Secchi depth values in S4 and S5 sectors are close to 0.5 m (Table 1), and even lower for areas close to the GB border [depth < 1.0 m, Fig. 1(b)].

A satisfactory agreement is observed between *in situ* and RG3-MERIS estimated Chl-*a* [Figs. 5(b)–5(f)]. The observed discrepancies can be associated with the high spatial variability
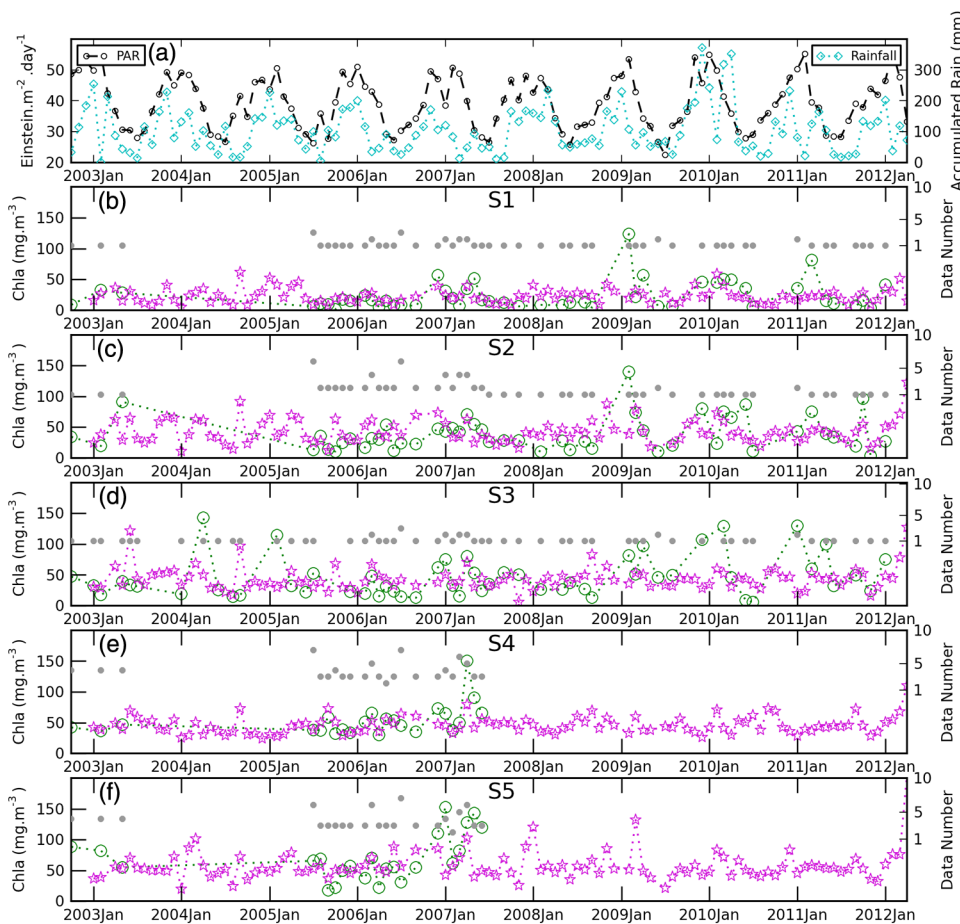

Fig. 5 (a) PAR and accumulated rainfall. *In situ* monthly Chl-*a* averages (green circles) and MERIS-estimated Chl-*a* (violet star) for the sectors: (b) S1, (c) S2, (d) S3, (e) S4, and (f) S5. The green squares show the number of samples used to calculate the *in situ* average.

of Chl-*a*, even within a same sector, and the differences in calculating the average values. For *in situ* data, a discrete sum of points was used. In most cases, there is only one sample per month. For MERIS data, an integration of pixels with 5 or more images was used. The highest differences are noted in the wet season, also characterized by higher spatial variability of Chl-*a*, as seen on Figs. 5(b)–5(f) and from *in situ* Chl-*a* standard deviation (Table 1).

In the wet season, the horizontal and vertical gradients of temperature, salinity, and nutrients are more influenced by the river discharge, larger precipitation [Fig. 5(a)], higher solar incidence [Fig. 5(a)], and by the intrusion of shelf waters into the bay. Particularly, the intrusion of South Atlantic Central Water (SACW), caused by the wind pattern over the continental shelf, is an import source of nutrients to the region.[73–76] This dynamics increases the water column stratification and the optical complexity,[22,25,77] reflected in the primary productivity and particulate and dissolved organic matter concentrations.[33,58,68]

Coupled to the seasonal variability, the tide imposes spatial variations in temperature, salinity, turbidity, and nutrient concentrations generating short-term modulations of the circulation pattern in the bay.[24] The renewal of waters by the tidal cycle depends on the distance to the mouth, the rivers runoff, and the local topography. The tidal channel (Fig. 1) has a key role in this process. Close to the mouth of the bay (sectors S1 and S2), surface currents are more intense[23] (1.6 m s⁻¹) in association with lowest Chl-*a* (Fig. 6). Sectors S3, S4, and S5 have weaker surface current ($\sim$0.3 m s⁻¹), low dilution efficiency by ocean waters and higher monthly average Chl-*a* (Fig. 6), due to the availability of nutrients that enter the bay as sewage. As pointed by Cotovicz et al.,[78] the most confined part of the inner bay behaved as the "bloom genesis region" that can spread phytoplankton production and biomass over the rest of the GB estuarine system.

Figures 6(a) and 6(b) show the monthly average values of *in situ* Chl-*a* and MERIS Chl-*a*, respectively, for S1, S2, S3, S4 and S5 sectors [Fig. 1(b)]. Despite some fluctuations, an *in situ* Chl-*a* decreasing (increasing) trend was observed from April to September (September to December). From January to March, the trend looks different among the sectors [Fig. 6(a)]. In January, the *in situ* Chl-*a* values increased at S3, S4, and S5 sectors as compared with
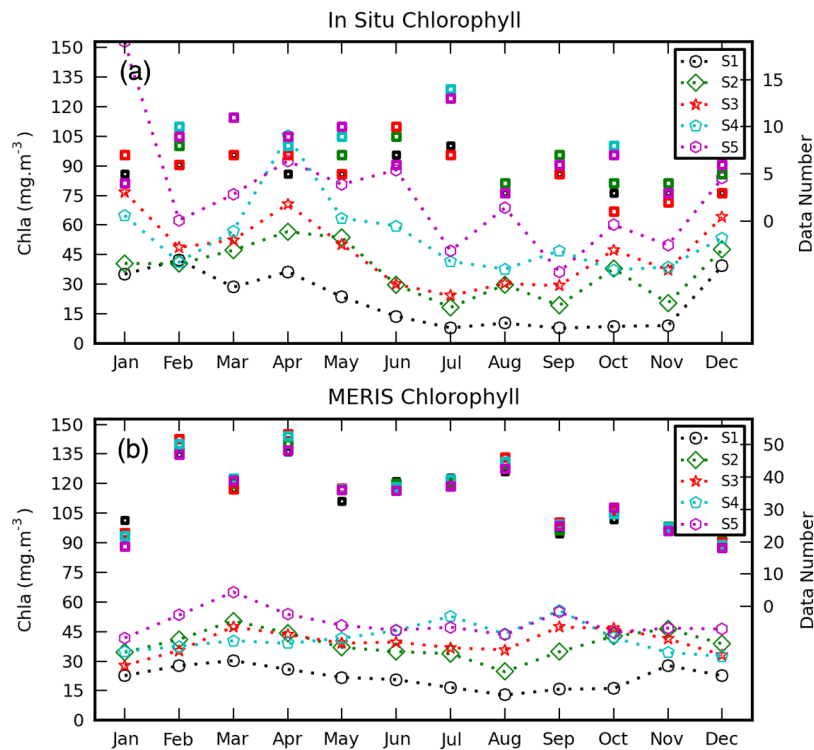

Fig. 6 (a) Climatological *in situ* Chl-*a* (b) and MERIS estimated Chl-*a* for sectors S1, S2, S3, S4, and S5 (see Fig. 1). Period: 2003 to 2012. The right *Y* axis shows the number of observations used to calculate the mean (squares in the graphs).

December, while at S1 and S2 sectors, the values decreased. Except for sector S1, the *in situ* Chl-*a* values increased from February to April [Fig. 6(a)]. The maximum *in situ* Chl-*a* values were found in April, except for sector S5, that had maximum value in January. The minimum *in situ* Chl-*a* values were observed in July (S1, S2, and S3 sectors), September (S5 sector), and October (S4 sector). The sampling rates of field measurements (*in situ* Chl-*a*) were generally below 10 samples per month [Fig. 6(a), right *Y* axis].

The MERIS Chl-*a* values [Fig. 6(b)] showed some similarity with *in situ* Chl-*a* values [Fig. 6(a)], particularly for S1 and S2 sectors. For S3, S4, and S5 sectors, the MERIS Chl-*a* values varied much less among the months when compared with the *in situ* Chl-*a* values. For S3 and S4 sectors, the maximum MERIS Chl-*a* values were estimated in September [Fig. 6(b)], in contrast with *in situ* Chl-*a* values [Fig. 6(a)], which showed lower values in September for these two sectors. The maximum MERIS Chl-*a* values were estimated in March for S1, S2, and S5 sectors. The sampling rates provided by MERIS imagery were more than 20 images per month [Fig. 6(b), right *Y* axis].

The RG3 algorithm was applied to a MERIS image time-series allowing the calculation of climatological monthly means of surface Chl-*a*. Figure 8 shows the spatial and temporal variability of monthly means MERIS Chl-*a* for all sectors [Fig. 1(b)]. As previously mentioned, lowest values are located in the tidal channel (S1 and S2 sectors), whereas higher concentrations (Chl-*a* > 70 mg m^{-3}) are observed in marginal regions, mainly in the S4 and S5 sectors (Fig. 8). S4 and S5 are the most impacted sectors by the river intake and urban/industrial outfalls. S3 sector is influenced by general GB dynamics and, consequently, has its productivity modulated by the water exchange with the other sectors (Fig. 8).

Relatively low MERIS Chl-*a* is observed in all sectors in January [Figs. 6(b) and 8(a)], in association with typical austral summer environmental conditions, such as high precipitation rate (Fig. 7), higher river discharges (not available), and wind regime that promote resuspension in the coastal area.[22] The rainy season is also cloudy limiting the acquisition of optical satellite imagery during this period. Consequently, there is a reduction in the availability of remote sensing data for "match-ups" with the *in situ* data. In the present study, 46 and 116 match-ups were obtained during the wet and dry seasons respectively (Table 2).

It is interesting to note a decrease in precipitation and an increase in light availability in February, followed by a slight increase in precipitation in March (Fig. 7). These relatively more stable environmental conditions, compared to the January conditions, seem to stimulate phytoplankton bloom, particularly in sector S5, when the MERIS Chl-*a* are considered [Figs. 8(b) and 8(c)]. Analyzing the extreme values, eight extreme values were identified in the *in situ* Chl-*a* time series with values > 500.0 mg m^{-3} (Sec. 5.1), with three (3) of those occurring in February and three (3) in March. Other extreme values of *in situ* Chl-*a* occurred in January (1) and September (1). In other words, the highest frequency of extreme values was not observed in January.
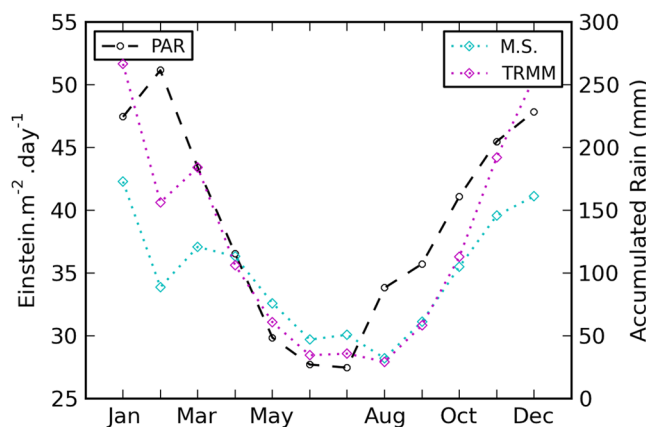

Fig. 7 Climatological variation of the PAR and precipitation in the Guanabara Bay watershed. M.S. = meteorological station rainfall (mean of two stations, see Fig. 1), TRMM = satellite derived rainfall. Period 2002 to 2012.
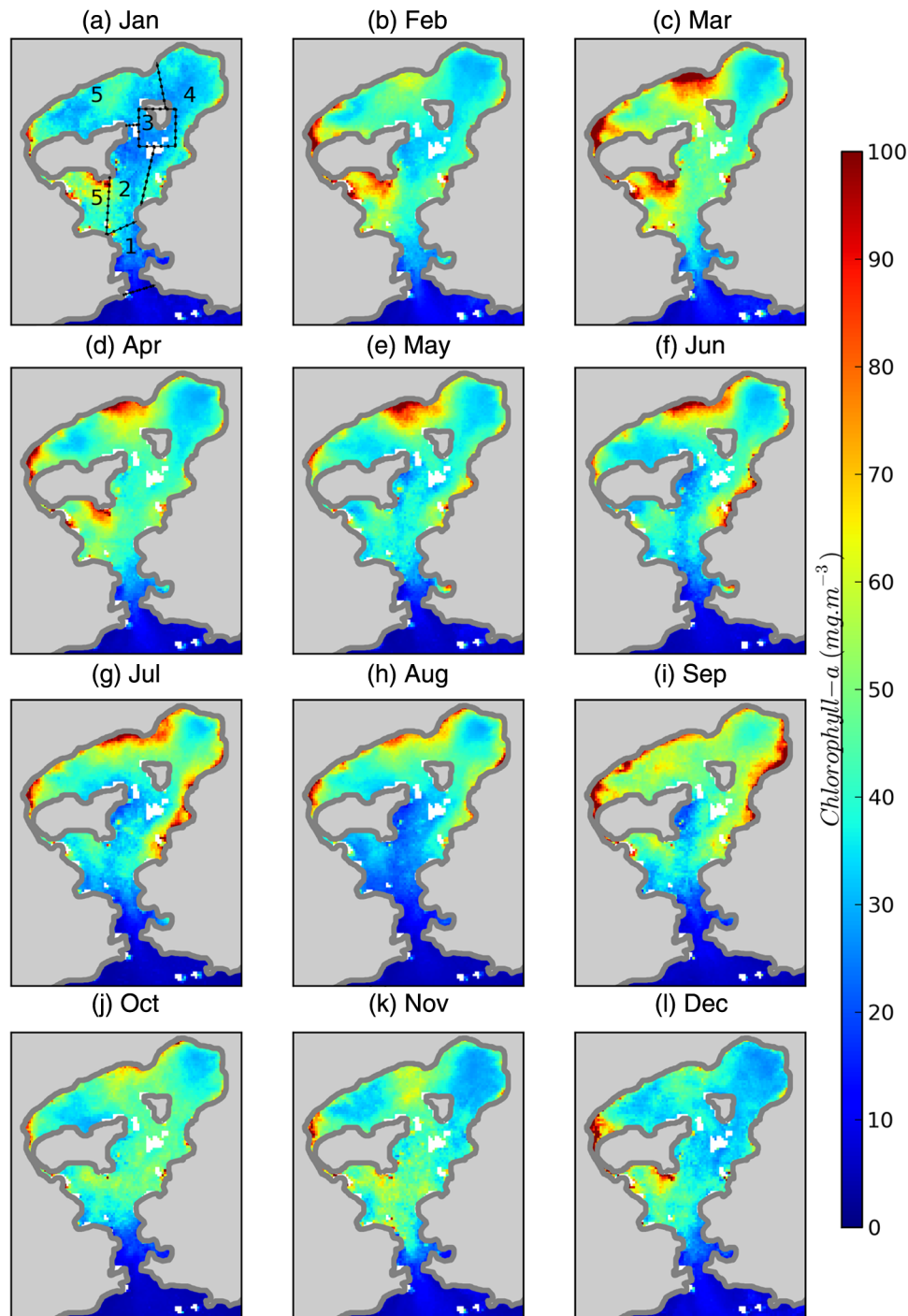
Fig. 8 Climatological (January 2003 to April 2012) monthly mean Chl-*a* (mg m^{-3}) distribution in Guanabara Bay, derived from MERIS images using the empirical algorithm RG3 (Chl-*a* = 62.565 $*$ $x^{1.6118}$). White spots mask the presence of exposed rocks on the water surface. The sectors cited in the text are indicated in (a).

High Chl-*a* are also observed in the northwest region of sector S4 and in the northeast region of sector S5, mainly from March to July. In early autumn (April) and Spring (September) [Figs. 8(d) and 8(i)], Chl-*a* values are still high in all sectors (except on sector S1), even in the dry season. April and September represent transition periods between dry and wet season. For S1 and S2 sectors, the lower Chl-*a* values are observed in August [Fig. 8(h)], when rainfall is also lower (Fig. 7). In the Guapimirim region (Fig. 1), northeast of sector S4, there is a pattern of

relatively constant Chl-*a* throughout the year ($\sim$30 mg m^{-3}). This trend was also observed by other authors,[22] who reported an average Chl-*a* value of 27 mg m^{-3}. According to these authors, the mangrove region located in the Guapimirim region acts as a barrier, filtering sediments and nutrients from the water column and keeping the Chl-*a* approximately constant.

6 Conclusion

An empirical algorithm that makes use of the red/green band ratio was calibrated from a set of *in situ* Chl-*a* concentrations and MERIS images allowing the estimation of a remotely sensed time-series of Chl-*a* for GB. Monthly means of Chl-*a* show seasonal patterns and spatial gradients that can be explained by the precipitation rate (river discharge), wind regime, light availability, tidal pump, local topography (estuary topology), stratification of the water column and discharge of untreated domestic and industrial wastes. In general, larger concentrations are observed in the wet season. However, high concentrations are also found during the months of April and September, transition periods between dry and wet seasons. The increasing anthropogenic interference in the GB watershed introduces more complexity in the spatial patterns of Chl-*a* concentrations. Thus, even in the dry season, high Chl-*a* are found in the marginal regions next to the spots of domestic and industrial sewage outfalls, mainly located in the GB eastern and western borders. Depending on the hydrodynamic regime, these high concentrations may be transported to more central areas.

It is expected that this study motivates further studies to obtain a more detailed knowledge of the optical properties of GB leading to an improvement of the algorithms. Understanding how the optical properties of water are affected by major optical constituents is critical for a remote sensing monitoring strategy.[79] Nowadays, the complete lack of concomitant information on the optical properties (inherent and apparent) and the main active optical constituents limit the development of algorithms and restrict the validation of atmospheric correction procedures. The possibility of measuring the atmospheric correction is a decisive step to evaluate more appropriately the use of bio-optical algorithms that make use of the red and infrared spectrum bands.

Finally, new sensors, like the Ocean and Land Colour Instrument (OLCI) onboard on Sentinel-3[80] and Operational Land Imager (OLI) onboard on Landsat-8[81] are promising sensors for monitoring the coastal and enclosed regions, like GB.[35] Some recommendations are suggested in order to improve the observational capacity of ocean color sensors.[82] For instance, the ability of incorporating spectral classification of water masses and the use of blended algorithms that takes into account empirical and theoretical considerations about the optical properties and the optical active constituents of the aquatic environment.

Acknowledgments

References

1. A. Morel and L. Prieur, "Analysis of variations in ocean color," *Limnol. Oceanogr.* **22**, 709–722 (1977).
2. J. E. O'Reilly et al., "Ocean color chlorophyll a algorithms for SeaWiFS, OC2, and OC4: version 4," in *SeaWiFS Postlaunch Calibration and Validation Analyses, Part 3 NASA Tech. Memo. 2000-206892*, S. B. Hooker and E. R. Firestone, Eds., Vol. 11, pp. 8–22, NASA Goddard Space Flight Center, Greenbelt, Maryland (2000).

3. T. S. Moore, J. W. Campbell, and M. D. Dowell, "A class-based approach to characterizing and mapping the uncertainty of the MODIS ocean chlorophyll product," *Rem. Sens. Environ.* **113**, 2424–2430 (2009).

4. M. Wang, W. Shi, and J. Tang, "Water property monitoring and assessment for China's inland Lake Taihu from MODIS-Aqua measurements," *Rem. Sens. Environ.* **115**, 841–854 (2011).

5. IOCCG, "Remote sensing of ocean colour in coastal, and other optically complex waters," in *Report of the Int. Ocean Colour Coordinating Group 3*, S. Sathyendranath, Ed., p. 140 (2000).

6. H. R. Gordon, "Atmospheric correction of ocean color imagery in the earth observing system era," *J. Geophys. Res.* **102**(D14), 17081–17106 (1997).

7. A. Siegel et al., "Atmospheric correction of satellite ocean color imagery: the black pixel assumption," *Appl. Opt.* **39**(21), 3582–3591 (2000).

8. M. Wang and W. Shi, "The NIR-SWIR combined atmospheric correction approach for MODIS ocean color data processing," *Opt. Express* **15**, 15722–15733 (2007).

9. T. Schroeder et al., "Atmospheric correction algorithm for MERIS above case-2 waters," *Int. J. Remote Sens.* **28**, 1469–1486 (2007).

10. C. Jamet et al., "Comparison of three SeaWiFS atmospheric correction algorithms for turbid waters using AERONET-OC measurements," *Remote Sens. Environ.* **115**, 1955–1965 (2011).

11. C. Goyens, C. Jamet, and T. Schroeder, "Evaluation of four atmospheric correction algorithms for MODIS-Aqua images over contrasted coastal waters," *Rem. Sens. Environ.* **131**, 63–75 (2013).

12. Q. He and C. Chen, "New approach for atmospheric correction of MODIS imagery in turbid coastal waters: a case study for the Pearl River Estuary," *Remote Sens. Lett.* **5**(3), 249–257 (2014).

13. IOCCG. "Remote sensing of inherent optical properties: fundamentals, tests of algorithms, and applications," in *Report of the Int. Ocean Colour Coordinating Group 5*, Z. P. Lee, Ed., p. 126 (2006).

14. P. J. Werdell et al., "Generalized ocean color inversion model for retrieving marine inherent optical properties," *Appl. Opt.* **52**, 2019–2037 (2013).

15. R. J. W. Brewin et al., "The ocean colour climate change initiative: III. A round-robin comparison on in-water bio-optical algorithms," *Remote Sens. Environ.* **162**, 271–294 (2015).

16. W. J. Moses et al., "Operational MERIS-based NIR-red algorithms for estimating chlorophyll-a concentrations in coastal waters - the Azov Sea case study," *Remote Sens. Environ.* **121**, 118–124 (2012).

17. F. Le et al., "Towards a long-term chlorophyll-a data record in a turbid estuary using MODIS observations," *Prog. Oceanogr.* **109**, 90–103 (2013).

18. F. Le et al., "Evaluation of chlorophyll-a remote sensing algorithms for an optically complex estuary," *Remote. Sens. Environ.* **129**, 75–89, (2013).

19. I. Ioannou et al., "Algorithms for the remote estimation of chlorophyll-a in the Chesapeake Bay," *Proc. SPIE* **9111**, 911118 (2014).

20. S. Novoa et al., "Water quality monitoring in Basque coastal areas using local chlorophyll-a algorithm and MERIS images," *J. Appl. Remote Sens.* **6**(1), 063519 (2012).

21. D. Blondeau-Partissier et al., "A review of ocean color remote sensing methods and statistical techniques for the detection, mapping and analysis of phytoplankton blooms in coastal and open oceans," *Prog. Oceanogr.* **123**, 123–144 (2014).

22. B. Kjerfve et al., "Oceanographic characteristics of an impacted coastal bay: Baía de Guanabara, Rio de Janeiro, Brazil," *Cont. Shelf Res.* **17**(13), 1609–1643 (1997).

23. L. Bérgamo, "Características hidrográficas da circulação e dos transportes do volume de sal na Baía de Guanabara (RJ): variações sazonais e moduladas pela maré," PhD Thesis, p. 200 (2006).

24. L. M. Mayr et al., "Hydrobiological characterization of Guanabara Bay," in *Hidrobiological Characterization of Guanabara Bay*, O. Magoon and C. Neves, Eds., pp. 124–138, American Society of Civil Engineers, New York (1989).

25. R. Paranhos, A. P. Pereira, and L. M. Mayr, "Diel variability of water quality in a tropical polluted bay," *Environ. Monit. Assess.* **50**, 131–141 (1998).

26. R. Paranhos et al., "Coupling bacterial abundance with production in a polluted tropical polluted coastal bay," in *Aquatic Microbial Ecology in Brazil*, B. M. Faria, V. F. Farjalla, and F. A. Esteves, Eds., Serie Oecologia Brasiliensis, Vol. **9**, pp. 117–132, PPGE-UFRJ, Brazil (2001).

27. D. Del Castillo and R. L. Miller, "On the use of ocean color remote sensing to measure the transport of dissolved organic carbon by the Mississippi River plume," *Remote Sens. Environ.* **112**(3), 836–844 (2008).

28. R. Miller and B. A. McKee, "Using MODIS Terra 250 m imagery to map concentrations of total suspended matter in coastal waters," *Remote Sens. Environ.* **93**(1), 59–266 (2004).

29. G. Dekker, V. Brando, and J. M. Anstee, "Retrospective seagrass change detection in a shallow coastal tidal Australian lake," *Remote Sens. Environ.* **97**, 415–433 (2005).

30. M. J. Moreno-Madrinan et al., "Using the surface reflectance MODIS Terra product to estimate turbidity in Tampa Bay, Florida," *Remote Sens.* **2**, 2713–2728 (2010).

31. C. Hu et al., "Moderate resolution imaging spectroradiometer (MODIS) observations of cyanobacteria blooms in Taihu Lake, China," *J. Geophys. Res.* **115**, C044002, (2010).

32. E. Siswanto et al., "Empirical ocean-color algorithms to retrieve chlorophyll-a, total suspended matter, and colored dissolved organic matter absorption coefficient in the Yellow and East China Seas," *J. Oceanogr.* **67**(5), 627–650 (2011).

33. Z. F. Braga, A. W. Setzer, and L. D. Lacerda, "Water quality assessment with simultaneous Landsat-5 TM data at Guanabara Bay, Rio de Janeiro, Brazil," *Remote Sens. Environ.* **45**, 95–106 (1993).

34. R. S. Barros et al., "Estimativa de turbidez e temperatura da água a partir de dados dos sensores TM e ETM+ para a baía de Guanabara," in *Anais XI Simpósio Brasileiro de Sensoriamento Remoto*, Belo Horizonte, Brasil, 05 to 10 April 2003, Instituto Nacional de Pesquisas Espaciais, pp. 2435–2442 (2003).

35. P. Roy et al., "Landsat-8: science and product vision for terrestrial global change research," *Remote Sens. Environ.* **145**, 154–172 (2014).

36. Rodolfo Paranhos, "Microbial observatory of Rio de Janeiro," www.biologia.ufrj.br/labs/hidrobiologia.

37. T. R. Parsons, Y. Maita, and C. M. Lalli, *A Manual of Chemical and Biological Methods for Seawater Analysis*, p. 173, Pergamon Press, Oxford (1984).

38. S. P. Paiva, "Análise da confiabilidade metrológica na determinação de pigmentos em ambientes marinhos por espectrofotometria," Master's Thesis, p. 98, Rio de Janiero, Brazil (2001).

39. National Aeronautics and Space Administration (NASA), "Giovanni—the bridge between data and science," http://disc.sci.gsfc.nasa.gov/giovanni (24 August 2015).

40. European Space Agency (ESA), "Coast colour project," http://www.coastcolour.org/.

41. H. Schiller and R. Doerffer, "Improved determination of coastal water constituent concentrations from MERIS data," *IEEE Trans. Geosci. Remote Sens.* **43**(7), 1585–1591 (2005).

42. R. Doerffer and H. Schiller, *MERIS Regional Coastal and Lake Case 2 Water Project - Atmospheric Correction ATBD, Version 1.0 18*, GKSS Research Center, Geesthacht, Germany (2008).

43. European Sapce Agency (ESA), "BEAM—earth observation toolbox and development platform," http://www.brockmann-consult.de/cms/web/beam/.

44. Python Software Foundation, "Python language reference—version 2.7," http://www.python.org/

45. J. F. R. Gower, R. Doerfer, and G. A. Bostard, "Interpretation of the 685 nm peak in water-leaving radiance in terms of fluorescence, absorption and scattering, and its observation by MERIS," *Int. J. Remote Sens.* **20**, 1771–1786 (1999).

46. J. F. R. Gower et al., "The use of the 709 nm band of MERIS to detect intense plankton blooms and other conditions in coastal waters," in *Proc. of the 2004 Envisat & ERS Symp. (ESA SP-572)*, Salzburg, Austria, H. Lacoste and L. Ouwehand, Eds., published on CD-Rom (2005).

47. J. F. R. Gower et al., "The importance of a band at 709 nm for interpreting water-leaving spectral radiance," *Can. J. Remote Sens.* **34**(3), 287–295 (2008).

48. H. R. Gordon et al., "A semianalytic radiance model of ocean color," *J. Geophys. Res.* **93**, 10909–10924 (1988).

49. A. Gitelson et al., "A simple semi-analytical model for remote estimation of chlorophyll-a in turbid waters: validation," *Rem. Sens. Environ.* **112**(9), 3582–3593 (2008).

50. A. Gitelson, J. F. Schalles, and C. M. Hladik, "Remote chlorophyll-a retrieval in turbid, productive estuaries: chesapeake Bay case study," *Remote Sens. Environ.* **109**, 464–472 (2007).

51. G. Dall'Olmo and A. A. Gitelson, "Effect of bio-optical parameter variability on the remote estimation of chlorophyll-a concentration in turbid productive waters: experimental results," *Appl. Opt.* **44**(3), 412–422 (2005).

52. G. Dall'Olmo et al., "Assessing the potential of SeaWiFS and MODIS for estimating chlorophyll concentration in turbid productive waters using red and near-infrared bands," *Remote Sens. Environ.* **96**(2), 176–187 (2005).

53. L. Gallegos, D. L. Correll, and J. W. Pierce, "Modeling spectral diffuse attenuation, absorption, and scattering coefficients in a turbid estuary," *Limnol. Ceanogr.* **35**, 1486–1502 (1990).

54. A. Gitelson, "The peak near 700 nm on radiance spectra of algae and water: relationships of its magnitude and position with chlorophyll concentration," *Int. J. Rem. Sens.* **13**(17), 3367–3373 (1992).

55. R. Doerffer and H. Schiller, "The MERIS case 2 water algorithm," *Int. J. Rem. Sens.* **28**, 517–535 (2007).

56. T. Kutser, "Passive optical remote sensing of cyanobacteria and other intense phytoplankton blooms in coastal and inland waters," *Int. J. Remote Sens.* **30**(17), 4401–4425 (2009).

57. V. S. Santos et al., "Auto-and heterotrophic and filamentous bactéria of Guanabara Bay (RJ, Brazil): estimates of cell/filamento numbers versus carbono contente," *Braz. J. Oceanogr.* **55**(2), 133–143 (2007).

58. A. Kalas et al., "Molecular and isotopic characterization of the particulate organic matter from an eutrophic coastal bay in SE Brazil," *Cont. Shelf Res.* **29**, 2293–2302 (2009).

59. V. Vantrepotte et al., "Optical classification of contrasted coastal waters," *Remote Sens. Environ.* **123**, 306–323 (2012).

60. C. Giardino et al., "In situ measurements and satellite remote sensing of case 2 waters: first results from the Curonian Lagoon," *Oceanologia* **52**(2), 197–210 (2010).

61. W. J. Moses et al., "Satellite estimation of chlorophyll-a concentration using the red and NIR bands of MERIS– the Azov Sea case study," *IEEE Geosci. Remote Sens. Lett.* **6**(4), 845–849 (2009).

62. T. Schroeder et al., "Atmospheric correction algorithm for MERIS above case-2 waters," *Int. J. Remote Sens.* **28**, 1469–1486 (2007).

63. L. Qi et al., "A novel MERIS algorithm to derive cyanobacterial phycocyanin pigment concentrations in a eutrophic lake: theoretical basis and practical considerations," *Remote Sens. Environ.* **154**, 298–317 (2014).

64. IOCCG, "Status and plans for satellite ocean-colour missions: considerations for complementary missions," in *Report of the Int. Ocean Color Coordinating Group 2*, J. A. Yoder, Ed., p. 43, IOCCG, Dartmouth, Canada (1999).

65. M. Kishino, S. Sugihara, and N. Okami, "Estimation of quantum yield of chlorophyll a fluorescence from the upward irradiance spectrum in the sea," *La Mer* **22**, 233–240 (1984).

66. A. Bricaud et al., "Variability in the chlorophyll-specific absorption coefficients of natural phytoplankton: analysis and parameterization," *J. Geophys. Res.* **100**, 13321–13332 (1995).

67. A. Gilerson et al., "Algorithms for remote estimation of chlorophyll-a in coastal and inland waters using red and near infrared bands," Papers in Natural Resources. Paper 286 (2010), http://digitalcommons.unl.edu/natrespapers/286 (15 December 2015).

68. M. C. Villac and D. R. Tenenbaum, "The phytoplankton of Guanabara Bay, Brazil. I. Historical account of its biodiversity," *Biota Neotrop.* **10**(2), 271–293 (2010).

69. M. Tzortziou et al., "Remote sensing reflectance and inherent optical properties in the mid Chesapeake Bay," *Estuarine Coastal Shelf Sci.* **72**, 16–32 (2007).

70. D. Doxaran, J. M. Froidefond, and P. Castaing, "Remote sensing reflectance of turbid sediment dominated waters. Reduction of sediment type variation and changing illumination condition effects by using of reflectance ratios," *Appl. Opt.* **42**, 2623–2634 (2003).

71. F. Shen, Y. X. Zhou, and G. L. Hong, "Absorption property of non-algal particles and contribution to total light absorption in optically complex waters: a case study in Yangtze Estuary and adjacent coast," in *Advances in Computational Environment Science*, G. Lee, Ed., Vol. **142**, pp. 61–66, Springer-Verlag Berlin, Heidelberg (2012).

72. F. Le et al., "Inherent and apparent optical properties of the complex estuarine waters of Tampa Bay: what controls light?," *Estuarine Coastal Shelf Sci.* **117**, 54–69 (2013).

73. S.H. Franchito et al., "Interaction between coastal upwelling and coastal winds at Cabo Frio, Brazil: an observational study," *J. Appl. Meteorol. Climatol.* **47**, 1590–1598 (2008).

74. R. Castelão and J. Barth, "Upwelling around Cabo Frio, Brazil: the importance of wind stress curl," *Geophys. Res. Lett.* **33**, L03602 (2006).

75. J. L. Valentin, D. J. Andre, and S. A. Jacob, "Hydrobiology in the Cabo Frio (Brazil) upwelling: two-dimensional structure and variability during a wind cycle," *Cont. Shelf Res.* **7**(1), 77–88 (1987).

76. E. N. Oliveira et al., "Entrada da ACAS na Baia de Guanabara (RJ)," in *X Simpósio Sobre Ondas, Marés, Engenharia Oceânica e Oceanografia por Satélite (X OMARSAT)*, Rio de Janeiro, Brazil (2013).

77. R. Paranhos et al., "Temperature and salinity trends in Guanabara Bay (Brazil) from 1980 to 1990," *Arquivos de Biologia e Tecnologia* **36**(4), 685–694 (1993).

78. L. C. Cotovicz, Jr. et al., "A large CO_2 sink enhanced by eutrophication in a tropical coastal embayment (Guanabara Bay, Rio de Janeiro, Brazil)," *Biogeosciences Discuss.* **12**, 4671–4720 (2015).

79. D. A. Aurin and H. M. Dierssen, "Advantages and limitations of ocean color remote sensing in CDOM-dominated, mineral-rich coastal and estuarine waters," *Remote Sens. Environ.* **125**, 181–197 (2012).

80. European Space Agency (ESA), "ESA earth online," https://earth.esa.int/web/guest/missions/esa-future-missions/sentinel-3 (12 January 2016).

81. U.S. Geological Survey, "Landsat missions," 1 December 2015, http://landsat.usgs.gov/landsat8.php (12 January 2016).

82. B. Mouw et al., "Aquatic color radiometry remote sensing of coastal and inland waters: challenges and recommendations for future satellite missions," *Remote Sens. Environ.* **160**, 15–30 (2015).

Eduardo Negri de Oliveira is the head of the Physical Oceanography Department at the Rio de Janeiro State University (UERJ). His main activities and interests are focused on remote sensing applied to oceanography.

Alexandro Macedo Fernandes received his bachelor's degree in physics from Federal University of Rio de Janeiro (1998), a master's degree in physical oceanography from University of São Paulo (2001) and a PhD degree in physical oceanography, Florida State University (2007). Currently, he works as faculty of the Physical Oceanography Department at Rio de Janeiro State University (UERJ). His main activities and interests are focused on observations and modeling of estuary and shelf hydrodynamics, internal waves and mixing processes.

Milton Kampel received his PhD in oceanography. He is a senior researcher at INPE, Brazil. At the Coordination of Earth Observation, he served as the head of the Remote Sensing Division. He is the member of the science team of the Brazil-Argentina SABIA-Mar mission for the observation of the oceans and member of the IOCCG. As a faculty member of the graduate program in remote sensing at INPE, he develops applications of remote sensing, satellite data telemetry, and geotechnologies in oceanography and environmental fields.

Renato Campello Cordeiro received his bachelor's degree in biology (1989), master's degree and PhD in geosciences (1995). He is an associated professor at Fluminense Federal University.

Nilva Brandini received her bachelor's degree in biology (1995), master's degree in botany (2000), PhD in geosciences (2008) and postdoctoral in marine sciences (2010 to 2015). She develops projects related to primary productivity of coastal ecosystems.

Susana Beatriz Vinzon is an associated professor at the Federal University of Rio de Janeiro, lecturing and researching on hydrodynamics and sediment transport, with emphasis in cohesive sediments.

Renata Grassi received her bachelor's degree in oceanography from Paraná Federal University (UFPR, 2007 to 2011) and her master's degree in oceanography from State University of Rio de Janeiro (2012 to 2014). Her master's degree dissertation focused on the development of empirical algorithms to quantify the main optically active substances presents in Guanabara Bay. She has experience with environmental consulting, and in 2014, she started working with data analysis at Petrobras's Centre of Operational Oceanography, Rio de Janeiro, Brazil.

Fernando Neves Pinto is graduated in biological sciences (1995). He has experience in ecology, with emphasis on ecotoxicology.

Alessandro Fillipo graduated in oceanography at Rio de Janeiro State University—UERJ (1987), MSc (1997), and PhD (2003) in geosciences (geochemistry) at Universidade Federal Fluminense–UFF. He accumulated experience in coastal management and monitoring programs, oceanography of bays, coastal lagoons, estuaries, numerical modeling of flow and transport in coastal systems, sea level fluctuations at different scales, data base development. Currently, he is an adjunct professor at the Department of Physical Oceanography and Meteorology, School of Oceanography (UERJ).

Rodolfo Paranhos is the PI ahead of the "Microbial Observatory of Rio de Janeiro—MORio," which since 1997 has provided data on the water quality of Guanabara Bay.